SUPPLEMENTARY INFORMATION

Global architecture of F-actin cytoskeleton regulates cell shape-dependent endothelial mechanotransduction

Yue Shao[a], Jennifer M. Mann[a], Weiqiang Chen[a], and Jianping Fu[a, b, *]

[a]Department of Mechanical Engineering, University of Michigan, Ann Arbor, Michigan, USA;

[b]Department of Biomedical Engineering, University of Michigan, Ann Arbor, Michigan, USA.

*Correspondence should be addressed to J. F. (jpfu@umich.edu).

Supplementary Information:

SUPPLEMENTARY METHODS

Fabrication of Si masters and PDMS stamps

Si micropost masters were fabricated using photolithography and deep reactive ion etching (DRIE), following a protocol published previously.[1,2] Briefly, a 5× reduction step-and-repeat projection stepper (Nikon NSR2005i9, Nikon Precision Inc.) was used for patterning photoresist. DRIE was performed with an inductively coupled plasma deep reactive-ion etcher (ICP Deep Trench Etching Systems, Surface Technology Systems). Heights of Si microposts were controlled by varying etching time during DRIE. After stripping photoresist with Piranha solution (4:1 H_2SO_4 / H_2O_2), dimensions of Si microposts were measured by surface profilometry (Prometrix P-10, KLA-Tenco Co.) and scanning electron microscopy (JEOL6320FV; JEOL USA, Inc.). The diameter of Si microposts generated in this work was 1.83 μm, with the post height ranging from 2 - 12 μm.

Relief structures on Si masters for microcontact printing were designed with an edge-to-edge distance of 40 μm and a depth of 15 - 20 μm and were fabricated using photolithography and DRIE. The depth of relief structures were optimized, as too shallow the relief structures, collapse of stamp roof could occur during microcontact printing, whereas too tall the relief structures, surfaces of PDMS stamps became extremely hydrophobic and made it difficult to ink the stamp surface uniformly with adhesive proteins.[3]

Before replica molding, all Si masters were treated with an oxygen plasma (Harrick Plasma) for 2 min before silanized with (tridecafluoro-1,1,2,2,-tetrahydrooctyl)-1-trichlorosilane vapor (United Chemical Technology) for 2 hr under vacuum, to render the Si surface hydrophobic and facilitate subsequent release of PDMS from Si masters.

PDMS stamps for microcontact printing were generated by replica molding. PDMS prepolymer with the base/curing agent ratio of 20:1 (*w*/*w*) was poured over Si masters and baked at 70°C for 48 hr. Fully cured PDMS was peeled off from Si masters before cut into small pieces using razor blades.

Fabrication and functionalization of PDMS microposts on the PDMS basal membrane

The protocol used in this work for fabrication and functionalization of the PDMS micropost array integrated on the PDMS basal membrane was based on a similar method reported in our previous publications.[2,4,5] Briefly, it consisted of three different steps: fabrication of the PDMS micropost array on a thin PDMS film, functionalization of PDMS microposts with ECM proteins, and integration of the PDMS micropost array onto a large PDMS basal membrane (**Supplementary Fig. S1**).

Fabrication of the PDMS micropost array on a thin PDMS film. A thin film of PDMS (with the base/curing agent ratio of 10:1) was spin-coated onto a clean glass coverslip at 2,000 rpm for 30 sec. The coverslip was baked at 70°C for 48 hr, resulting in a fully cured thin PDMS film with a thickness of 20 µm. To fabricate the PDMS micropost array on the thin PDMS film, we first generated a negative PDMS template containing an array of holes, by pouring PDMS prepolymer (with the base/curing agent ratio of 10:1) over the Si micropost master. The negative PDMS template was cured at 110°C for 20 min, peeled off, oxidized with oxygen plasma and silanized with (tridecafluoro-1,1,2,2,-tetrahydrooctyl)-1-trichlorosilane vapor overnight under vacuum. To generate the final PDMS micropost array on the thin PDMS film, PDMS prepolymer was poured over the negative PDMS template and degassed under vacuum before the coverslip containing the PDMS thin film was flipped and put into direct contact with the negative template covered with PDMS prepolymer. A gentle force was applied to the coverslip to ensure horizontal and uniform contact between the coverslip and the negative template. The whole assembly was baked at 110°C for 20 hr, before the coverslip containing the PDMS micropost array was gently peeled off the template. When peeling induced collapse of the PDMS micropost arrays, we regenerated the arrays by sonication in 100% ethanol for 30 sec followed by dry-release with liquid CO_2 using a critical point dryer (Samdri-PVT-3D, Tousimis).

Functionalization of PDMS micropost top surfaces with ECM proteins. Functionalization of the PDMS micropost top surface was achieved using microcontact printing while the PDMS micropost array was still held on the coverslip. Briefly, PDMS stamps (either featureless or with patterned surface structures) were cleaned by sonication in 100% ethanol, blown dry under nitrogen gas and then immersed in a saturating fibronectin solution (30 - 50 µg ml^{-1}) for 1 hr. The PDMS stamps were washed three times in PBS and blown dry using nitrogen gas. Fibronectin coated PDMS stamps were placed in conformal contact with UV ozone-treated, surface-oxidized PDMS micropost array, to facilitate fibronectin transfer from the stamp to the PDMS micropost array.

Integration of the PDMS micropost array onto the basal PDMS membrane. To generate the basal PDMS membrane, PDMS prepolymer (with the base/curing agent ratio of 10:1) was spin-coated on 100-mm petri dish covers at 500 rpm for 30 sec before baked at 70°C for > 48 hr, which resulted in a fully cured PDMS membrane with a thickness of 200 - 300 μm. In parallel, the thin PDMS film holding the PDMS micropost array was gently peeled off the coverslip and was flipped and brought into conformal contact with a PDMS pad. It should be noted that the PDMS pad, which serves to protect the ECM proteins on the top surface of the PDMS micropost array, should be prepared freshly, so that its surface remains hydrophobic and has a low affinity to ECM proteins and thus will not adsorb ECM proteins from the PDMS microposts. To make sure conformal contact between the micropost tops and the PDMS pad, a gentle nitrogen blast over the backside of the thin PDMS film was found helpful. The backside of the PDMS thin film and the top surface of the PDMS basal membrane were both treated with oxygen plasma for 50 sec before permanently bonded together via plasma-assisted PDMS-PDMS bonding. The resultant PDMS micropost array on the PDMS basal membrane was immersed sequentially in 100%, 70% and 30% ethanol before submerged in DI water.

The PDMS microposts were fluorescently labeled with a 5 μg mL^{-1} Δ^9-DiI solution for 1 hr. After replacing DiI solution with DI water, passivation of the PDMS micropost array was performed by incubating in 0.2% Pluronic F-127 (BASF) for 30 min. This passivation step rendered the surface areas of the PDMS micropost array not coated with fibronectin resistant to protein adsorption, preventing cell adhesion to these undesired areas of the PDMS micropost array. The PDMS micropost array was then rinsed thoroughly with DI (before stored at 4°C for up to one week).

Before use, the PDMS micropost array was rinsed thoroughly with PBS, submerged in culture media, and pre-equilibrated at 37^{o}C in 5% CO_2.

Theoretical modeling of the F-actin cytoskeleton mechanics

In this study, we developed a mechanics model from first principles to recapitulate how the F-actin cytoskeleton architecture (**Fig. 4A & Supplementary Fig. S8A**) could regulate the response of CSK contractile forces under uniaxial stretch. Our theoretical model involved three configurations of the F-actin CSK for each cell morphology – a reference configuration, a pre-stressed configuration and a stretched configuration – defined as following.

The reference configuration (**Fig. 4B**) was defined as the initial configuration of the F-actin CSK wherein all the dimensions were known *a priori* and there was no strain or stress in the F-actin CSK structure (i.e., in a mechanically resting cell). For a living contractile cell, the pre-stressed configuration was reached by introducing the pre-strain, $\varepsilon_{\mathrm{pre}}$, into each F-actin fiber, and achieving a mechanical equilibrium wherein the anchorage (or FA)-mediated reactive forces F were in balance with the internal CSK tension T. After uniaxial stretch of 10% was applied to the cell, it reached another mechanical equilibrium – the stretched configuration – where the reactive forces were again in balance with the internal tensions (**Supplementary Fig. S8B-F**).

Since the pre-stressed and stretched configurations of the F-actin CSK were similar in topology, we only illustrated the latter in **Supplementary Fig. S8B-F** for the sake of clarity, and all the unknown variables in the pre-stressed configuration and those in the stretched configuration were differentiated only by a prime (’) on the top-right of the latter. In our model, each F-actin fiber was assumed to have the same mechanical property, constitutive law and pre-strain (equation (1)). As illustrated in our models (**Supplementary Fig. S8B-F**), except for the circular cell model, it was critical to solve for the position of each “Y” junctions in the model ($2x$, $2y$; $2x'$, $2y'$), in order to calculate the balanced reaction forces and internal tensions in both the pre-stressed configuration and the stretched configuration. Normalizing the reaction forces in the stretched configuration over those in the pre-stressed configuration resulted in the normalized response of cellular contractile forces, as a theoretical prediction that could be directly compared with our experimental data. In the following, we will present the explicit mathematical expressions of the theoretical model for each scenario (**Supplementary Fig. 8B-F**).

(1) For a circular cell (**Supplementary Fig. S8B**), the mathematical description has been provided in the main text.

(2) For a square cell (**Supplementary Fig. S8C**) under pre-stressed configuration, the four corners were considered as fixed boundary conditions, while the four Y-junctions were displaced off their positions in the reference configuration. According the symmetry, new positions of the

Y-junctions were determined by two unknown variable x and y. In the pre-stressed configuration, the internal tensions within the F-actin CSK were given by

$$T_1 = K\left(2+\varepsilon_{\mathrm{pre}}-\frac{6x}{\sqrt{2}a}\right)^2 \tag{S1}$$

$$T_2 = K\left(2+\varepsilon_{\mathrm{pre}}-\frac{6y}{\sqrt{2}a}\right)^2 \tag{S2}$$

$$T_3 = K\left(\frac{3\sqrt{x^2+y^2}}{\sqrt{2}a}-1+\varepsilon_{\mathrm{pre}}\right)^2 \tag{S3}$$

, where a = 50 μm. The mechanical equilibrium between T_1 and T_3 as well as between T_2 and T_3 resulted in

$$x = \frac{\sqrt{x^2+y^2}}{2}\left(\frac{2+\varepsilon_{\mathrm{pre}}-\dfrac{6x}{\sqrt{2}a}}{\dfrac{3\sqrt{x^2+y^2}}{\sqrt{2}a}-1+\varepsilon_{\mathrm{pre}}}\right)^2 \tag{S4}$$

$$y = \frac{\sqrt{x^2+y^2}}{2}\left(\frac{2+\varepsilon_{\mathrm{pre}}-\dfrac{6y}{\sqrt{2}a}}{\dfrac{3\sqrt{x^2+y^2}}{\sqrt{2}a}-1+\varepsilon_{\mathrm{pre}}}\right)^2 \tag{S5}$$

The x and y could then be solved using iteration method. They were then used to calculate the values for reaction forces F_1 and F_2 by

$$F_1 = T_1 = K\left(2+\varepsilon_{\mathrm{pre}}-\frac{6x}{\sqrt{2}a}\right)^2 \tag{S6}$$

$$F_2 = T_2 = K\left(2+\varepsilon_{\mathrm{pre}}-\frac{6y}{\sqrt{2}a}\right)^2 \tag{S7}$$

Due to the symmetry of the pre-stressed configuration before stretch, the reaction forces were found all identical to each other, i.e., $F_1 = F_2$. For a square cell in the stretched configuration under diagonal stretch (**Supplementary Fig. S8C**), the positions of the Y-junctions were determined in a way similar to that we discussed above. To be specific, the internal tensions within the F-actin CSK were given by

$$T_1' = K\left(2.3+\varepsilon_{\text{pre}}-\frac{6x'}{\sqrt{2}a}\right)^2 \tag{S8}$$

$$T_2' = K\left(2+\varepsilon_{\text{pre}}-\frac{6y'}{\sqrt{2}a}\right)^2 \tag{S9}$$

$$T_3' = K\left(\frac{3\sqrt{x'^2+y'^2}}{\sqrt{2}a}-1+\varepsilon_{\text{pre}}\right)^2 \tag{S10}$$

The mechanical equilibrium between T_1’ and T_3’ as well as between T_2’ and T_3’ resulted in

$$x' = \frac{\sqrt{x'^2+y'^2}}{2}\left(\frac{2.3+\varepsilon_{\text{pre}}-\frac{6x'}{\sqrt{2}a}}{\frac{3\sqrt{x'^2+y'^2}}{\sqrt{2}a}-1+\varepsilon_{\text{pre}}}\right)^2 \tag{S11}$$

$$y' = \frac{\sqrt{x'^2+y'^2}}{2}\left(\frac{2+\varepsilon_{\text{pre}}-\frac{6y'}{\sqrt{2}a}}{\frac{3\sqrt{x'^2+y'^2}}{\sqrt{2}a}-1+\varepsilon_{\text{pre}}}\right)^2 \tag{S12}$$

The x’ and y’ could then be solved using iteration method. They were then used to calculate the value for reaction force F_1’ and F_2’ by

$$F_1' = T_1' = K\left(2.3+\varepsilon_{\text{pre}}-\frac{6x'}{\sqrt{2}a}\right)^2 \tag{S13}$$

$$F_2' = T_2' = K\left(2+\varepsilon_{\text{pre}}-\frac{6y'}{\sqrt{2}a}\right)^2 \tag{S14}$$

, from which, in combination with equation (S6) and (S7), the normalized cellular force response (F_1’+F_2’)/(F_1+F_2) (**Fig. 4C**) and normalized subcellular force responses F_1’/F_1 and F_2’/F_2 (**Fig. 4D**) were predicted using $\varepsilon_{\text{pre}} = 0.25$.

(3) For a square cell (**Supplementary Fig. S8D**) in pre-stressed configuration, but in a coordinate system rotated 45 degrees from that shown in **Supplementary Fig. S8C**, the internal tensions were given by the positions of the Y-junctions:

$$T_1 = K\left(\frac{6\sqrt{\left(\frac{a}{2}-x\right)^2+\left(\frac{a}{2}-y\right)^2}}{\sqrt{2}a}-1+\varepsilon_{\text{pre}}\right)^2 \tag{S15}$$

$$T_2 = K\left(\frac{3y}{a}-1+\varepsilon_{\text{pre}}\right)^2 \tag{S16}$$

$$T_3 = K\left(\frac{3x}{a}-1+\varepsilon_{\text{pre}}\right)^2 \tag{S17}$$

The mechanical equilibrium between T_1, T_2 and T_3 resulted in

$$x = \frac{a}{2}-\sqrt{\left(\frac{a}{2}-x\right)^2+\left(\frac{a}{2}-y\right)^2}\left(\frac{\frac{3x}{a}-1+\varepsilon_{\text{pre}}}{\frac{6\sqrt{\left(\frac{a}{2}-x\right)^2+\left(\frac{a}{2}-y\right)^2}}{\sqrt{2}a}-1+\varepsilon_{\text{pre}}}\right)^2 \tag{S18}$$

$$y = \frac{a}{2}-\sqrt{\left(\frac{a}{2}-x\right)^2+\left(\frac{a}{2}-y\right)^2}\left(\frac{\frac{3y}{a}-1+\varepsilon_{\text{pre}}}{\frac{6\sqrt{\left(\frac{a}{2}-x\right)^2+\left(\frac{a}{2}-y\right)^2}}{\sqrt{2}a}-1+\varepsilon_{\text{pre}}}\right)^2 \tag{S19}$$

The x and y could then be solved using iteration method. They were then used to calculate the value for reaction forces F by

$$F = T_1 = K\left(\frac{6\sqrt{\left(\frac{a}{2}-x\right)^2+\left(\frac{a}{2}-y\right)^2}}{\sqrt{2}a}-1+\varepsilon_{\text{pre}}\right)^2 \tag{S20}$$

We found the result given by equation (S20) was identical to the results given by equation (S6) and (S7), because the pre-stressed configurations in both cases were physically the same, except for a rotation of the coordinate system. For the square cell in stretched configuration under stretch along the edge (**Supplementary Fig. S8D**), the internal tensions were

$$T_1' = K\left(\frac{6\sqrt{\left(\frac{1.1a}{2}-x'\right)^2+\left(\frac{a}{2}-y'\right)^2}}{\sqrt{2}a}-1+\varepsilon_{\text{pre}}\right)^2 \tag{S21}$$

$$T_2' = K\left(\frac{3y'}{a}-1+\varepsilon_{\text{pre}}\right)^2 \tag{S22}$$

$$T_3' = K\left(\frac{3x'}{a}-1+\varepsilon_{\text{pre}}\right)^2 \tag{S23}$$

The mechanical equilibrium between T_1', T_2' and T_3' resulted in

$$x' = \frac{1.1a}{2}-\sqrt{\left(\frac{1.1a}{2}-x'\right)^2+\left(\frac{a}{2}-y'\right)^2}\left(\frac{\frac{3x'}{a}-1+\varepsilon_{\text{pre}}}{\frac{6\sqrt{\left(\frac{1.1a}{2}-x'\right)^2+\left(\frac{a}{2}-y'\right)^2}}{\sqrt{2}a}-1+\varepsilon_{\text{pre}}}\right)^2 \tag{S24}$$

$$y' = \frac{a}{2}-\sqrt{\left(\frac{1.1a}{2}-x'\right)^2+\left(\frac{a}{2}-y'\right)^2}\left(\frac{\frac{3y'}{a}-1+\varepsilon_{\text{pre}}}{\frac{6\sqrt{\left(\frac{1.1a}{2}-x'\right)^2+\left(\frac{a}{2}-y'\right)^2}}{\sqrt{2}a}-1+\varepsilon_{\text{pre}}}\right)^2 \tag{S25}$$

The x' and y' could then be solved using iteration method. They were then used to calculate the value for reaction force F' by

$$F' = T_1' = K\left(\frac{6\sqrt{\left(\frac{1.1a}{2}-x'\right)^2+\left(\frac{a}{2}-y'\right)^2}}{\sqrt{2}a}-1+\varepsilon_{\text{pre}}\right)^2 \tag{S26}$$

, from which, in combination with equation (S20), the normalized cellular force response F'/F (**Fig. 4C**) was predicted using $\varepsilon_{\text{pre}} = 0.25$.

(4) For a rectangular cell (**Supplementary Fig. S8E**) in pre-stressed configuration, the internal tensions were given by

$$T_1 = K\left(\frac{6\sqrt{\left(\frac{L}{2}-x\right)^2+\frac{b^2}{36}}}{\sqrt{L^2+b^2}}-1+\varepsilon_{\text{pre}}\right)^2 \tag{S27}$$

$$T_2 = K\left(\frac{3x}{L}-1+\varepsilon_{\text{pre}}\right)^2 \tag{S28}$$

The mechanical equilibrium between T_1 and T_2 resulted in

$$x = \frac{L}{2}-\frac{\sqrt{\left(\frac{L}{2}-x\right)^2+\frac{b^2}{36}}}{2}\left(\frac{\frac{3x}{L}-1+\varepsilon_{\text{pre}}}{\frac{6\sqrt{\left(\frac{L}{2}-x\right)^2+\frac{b^2}{36}}}{\sqrt{L^2+b^2}}-1+\varepsilon_{\text{pre}}}\right)^2 \tag{S29}$$

The x could then be solved using iteration method. It was then used to calculate the value for reaction forces F by

$$F = T_1 = K\left(\frac{6\sqrt{\left(\frac{L}{2}-x\right)^2+\frac{b^2}{36}}}{\sqrt{L^2+b^2}}-1+\varepsilon_{\text{pre}}\right)^2 \tag{S30}$$

For a rectangular cell in the stretched configuration under longitudinal stretch (**Supplementary Fig. S8E**), the internal tensions were

$$T_1' = K\left(\frac{6\sqrt{\left(\frac{1.1L}{2}-x'\right)^2+\frac{b^2}{36}}}{\sqrt{L^2+b^2}}-1+\varepsilon_{\text{pre}}\right)^2 \tag{S31}$$

$$T_2' = K\left(\frac{3x'}{L}-1+\varepsilon_{\text{pre}}\right)^2 \tag{S32}$$

The mechanical equilibrium between T_1'and T_2' resulted in

$$x' = \frac{1.1L}{2} - \frac{\sqrt{\left(\frac{1.1L}{2} - x'\right)^2 + \frac{b^2}{36}}}{2}\left(\frac{\frac{3x'}{L} - 1 + \varepsilon_{\text{pre}}}{\frac{6\sqrt{\left(\frac{1.1L}{2} - x'\right)^2 + \frac{b^2}{36}}}{\sqrt{L^2 + b^2}} - 1 + \varepsilon_{\text{pre}}}\right)^2 \tag{S33}$$

The *x*’ could then be solved using iteration method. It was then used to calculate the value for reaction force *F*’ by

$$F' = T_1' = K\left(\frac{6\sqrt{\left(\frac{1.1L}{2} - x'\right)^2 + \frac{b^2}{36}}}{\sqrt{L^2 + b^2}} - 1 + \varepsilon_{\text{pre}}\right)^2 \tag{S34}$$

, from which , in combination with equation (S30), the normalized cellular force response *F*’/*F* (**Fig. 4C**) was predicted using $\varepsilon_{\text{pre}} = 0.25$.

(5) For a rectangular cell in the stretched configuration under transverse stretch (**Supplementary Fig. S8F**), the internal tensions were

$$T_1' = K\left(\frac{6\sqrt{\left(\frac{L}{2} - x'\right)^2 + \frac{1.21}{36}b^2}}{\sqrt{L^2 + b^2}} - 1 + \varepsilon_{\text{pre}}\right)^2 \tag{S35}$$

$$T_2' = K\left(\frac{3x'}{L} - 1 + \varepsilon_{\text{pre}}\right)^2 \tag{S36}$$

The mechanical equilibrium between T_1’and T_2’ resulted in

$$x' = \frac{L}{2} - \frac{\sqrt{\left(\frac{L}{2} - x'\right)^2 + \frac{1.21}{36}b^2}}{2}\left(\frac{\frac{3x'}{L} - 1 + \varepsilon_{\text{pre}}}{\frac{6\sqrt{\left(\frac{L}{2} - x'\right)^2 + \frac{1.21}{36}b^2}}{\sqrt{L^2 + b^2}} - 1 + \varepsilon_{\text{pre}}}\right)^2 \tag{S37}$$

The x' could then be solved using iteration method. It was then used to calculate the value for reaction force F' by

$$F' = T_1' = K\left(\frac{6\sqrt{\left(\frac{L}{2}-x'\right)^2+\frac{1.21}{36}b^2}}{\sqrt{L^2+b^2}}-1+\varepsilon_{\mathrm{pre}}\right)^2 \tag{S38}$$

, from which, in combination with equation (S30), the normalized cellular force response F'/F (**Fig. 4C**) was predicted using $\varepsilon_{\mathrm{pre}} = 0.25$.

REFERENCES

1. J. Fu, Y.-K. Wang, M. Yang, R. Desai, X. Yu, Z. Liu and C. Chen, *Nat. Methods*, 2010, **7,** 733.

2. M. Yang, J. Fu, Y.-K. Wang, R. Desai and C. Chen, *Nat. Protoc.*, 2011, **6,** 187.

3. D. Qin, Y. Xia and G. Whitesides, *Nat. Protoc.*, 2010, **5,** 491.

4. J. Mann, R. Lam, S. Weng, Y. Sun and J. Fu, *Lab Chip*, 2012, **12,** 731.

5. R. Lam, S. Weng, W. Lu and J. Fu, *Integr. Biol.*, 2012, **4,** 1289.

SUPPLEMENTARY FIGURES WITH CAPTIONS

Supplementary Figure S1

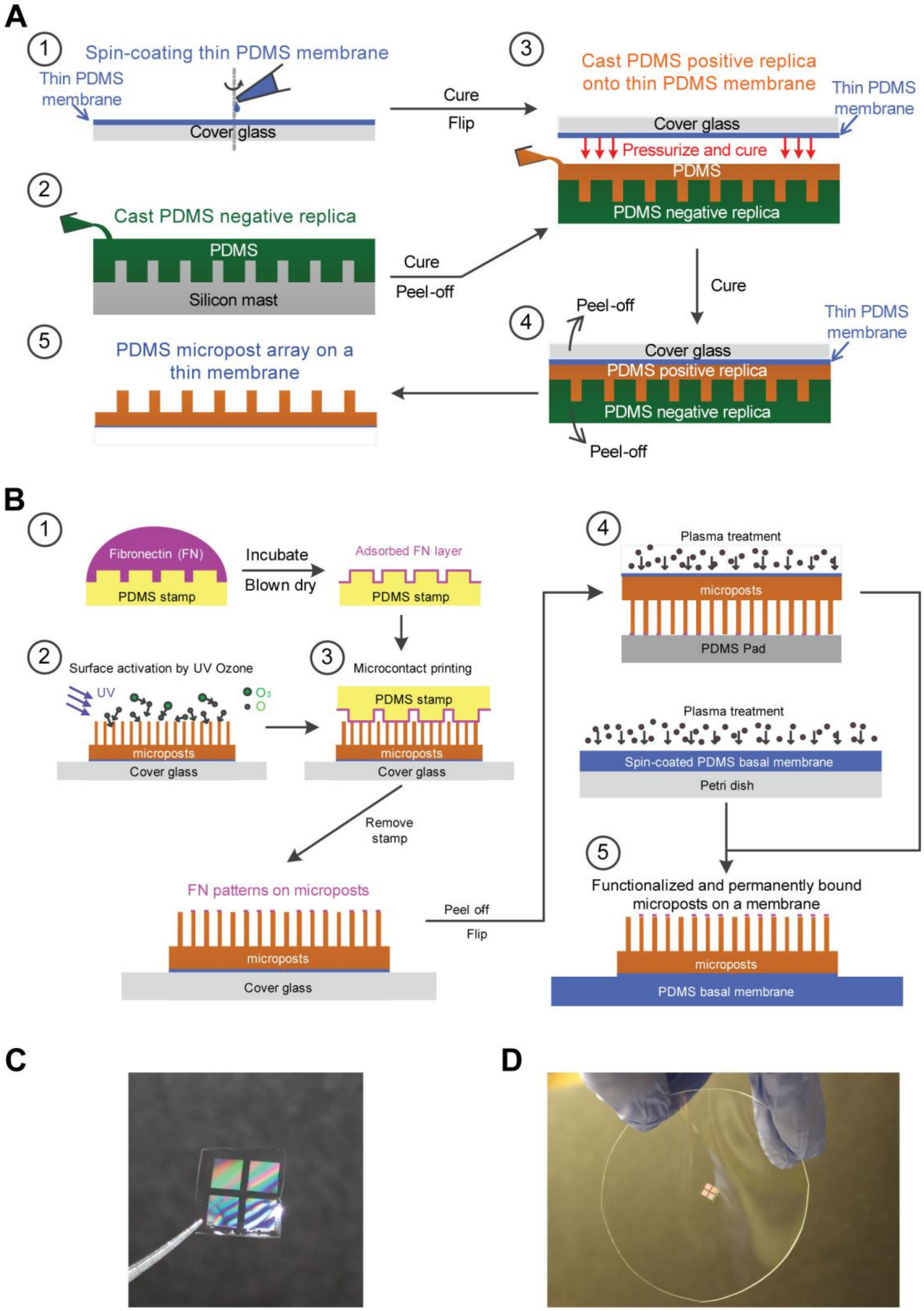

Supplementary Fig. S1. Fabrication, functionalization and integration of PDMS microposts on a stretchable PDMS membrane. (**A**) Detailed fabrication process for the PDMS micropost array on a thin PDMS film. See **SI text** for detailed description. (**B**) Functionalization (step 1 - 3) and integration (step 4 - 5) of the PDMS micropost array onto a stretchable PDMS basal membrane. See **SI text** for detailed description. (**C&D**) Photographs of the PDMS micropost array on a free-standing PDMS thin film (**C**) before bonded onto the stretchable PDMS basal membrane (**D**).

Supplementary Figure S2

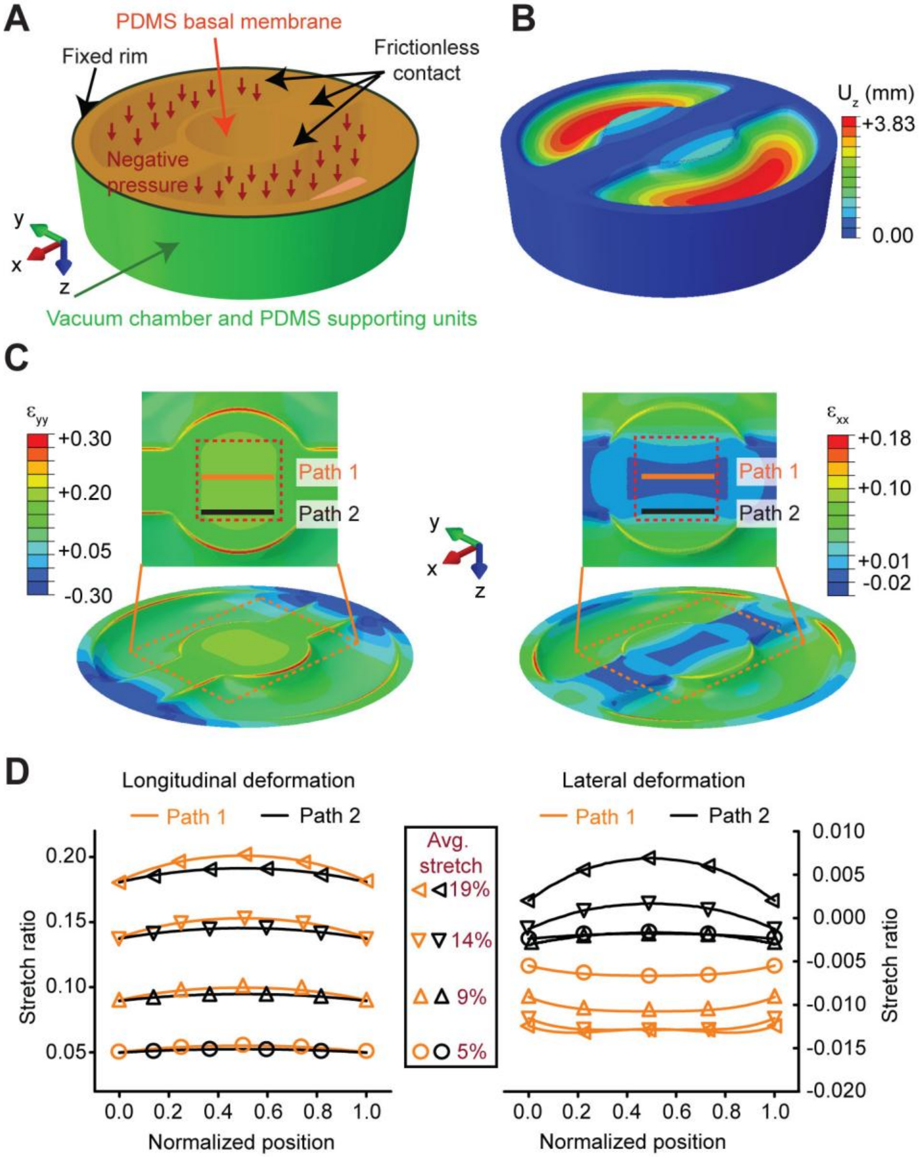

Supplementary Fig. S2. Finite element (FE) modeling of uniaxial stretch by the CSD. (**A**) Three-dimensional (3D) computer-aided engineering (CAE) model of the uniaxial CSD. The PDMS membrane was in a frictionless contact with the base supporting unit of the CSD. The outer rim of the PDMS membrane was affixed to the CSD. Negative pressure was applied on the part of PDMS membrane resting on the top of two vacuum compartments. (**B**) FE simulation result of the vertical (*z*-axis) displacement field within the PDMS membrane under vacuum. (**C**) FE simulation results of the longitudinal (*y*-axis) (*left*) and lateral (*x*-axis) (*right*) tensile strain fields within the PDMS membrane under vacuum. Insets show magnified views for the tensile strain fields within the central region (*marked by dashed rectangles*) of the PDMS membrane, on which the PDMS micropost array was integrated. Two different paths within the central region of the membrane were selected, with the stretch ratio along each path plotted in **D**. (**D**) Plots of longitudinal (*left*) and lateral (*right*) stretches along the two paths selected in **C**, under different levels of average uniaxial stretches. Please note that the vertical axes for the longitudinal (*left*) and lateral (*right*) stretches had different scales. It was clear that the lateral stretch was much less than the longitudinal stretch, demonstrating high directionality of uniaxial stretch achieved by the CSD.

Supplementary Figure S3

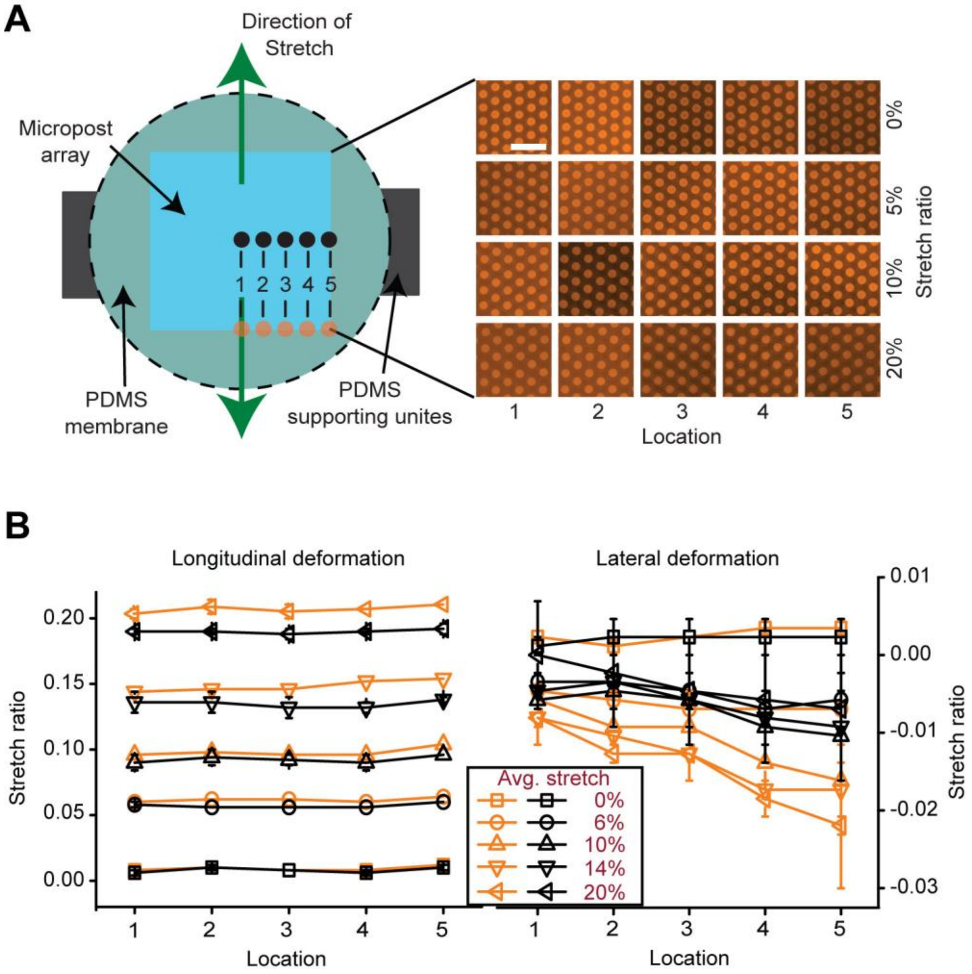

Supplementary Fig. S3. Experimental characterization of uniaxial stretch by the CSD. (**A**) (*Left*) Schematic of characterization. Two sets of 5 different locations on the PDMS basal membrane along the two paths marked in **Supplementary Fig. S2C** were selected to quantify the uniformity and directionality of uniaxial stretch (*green arrows*). (*Right*) Fluorescence images of the PDMS micropost array at the 5 locations (*black dots*) along the center line of the PDMS membrane under different levels of uniaxial stretch. Longitudinal and lateral stretch ratios were quantified by calculating the change of micropost center-center distance after stretch. Scale bar, 10 μm. (**B**) Plots of longitudinal (*left*) and lateral (*right*) stretch ratios as a function of different locations marked in **A** along the two different paths under different levels of average stretch. Data represents the mean ± standard error (*S.D.*).

Supplementary Figure S4

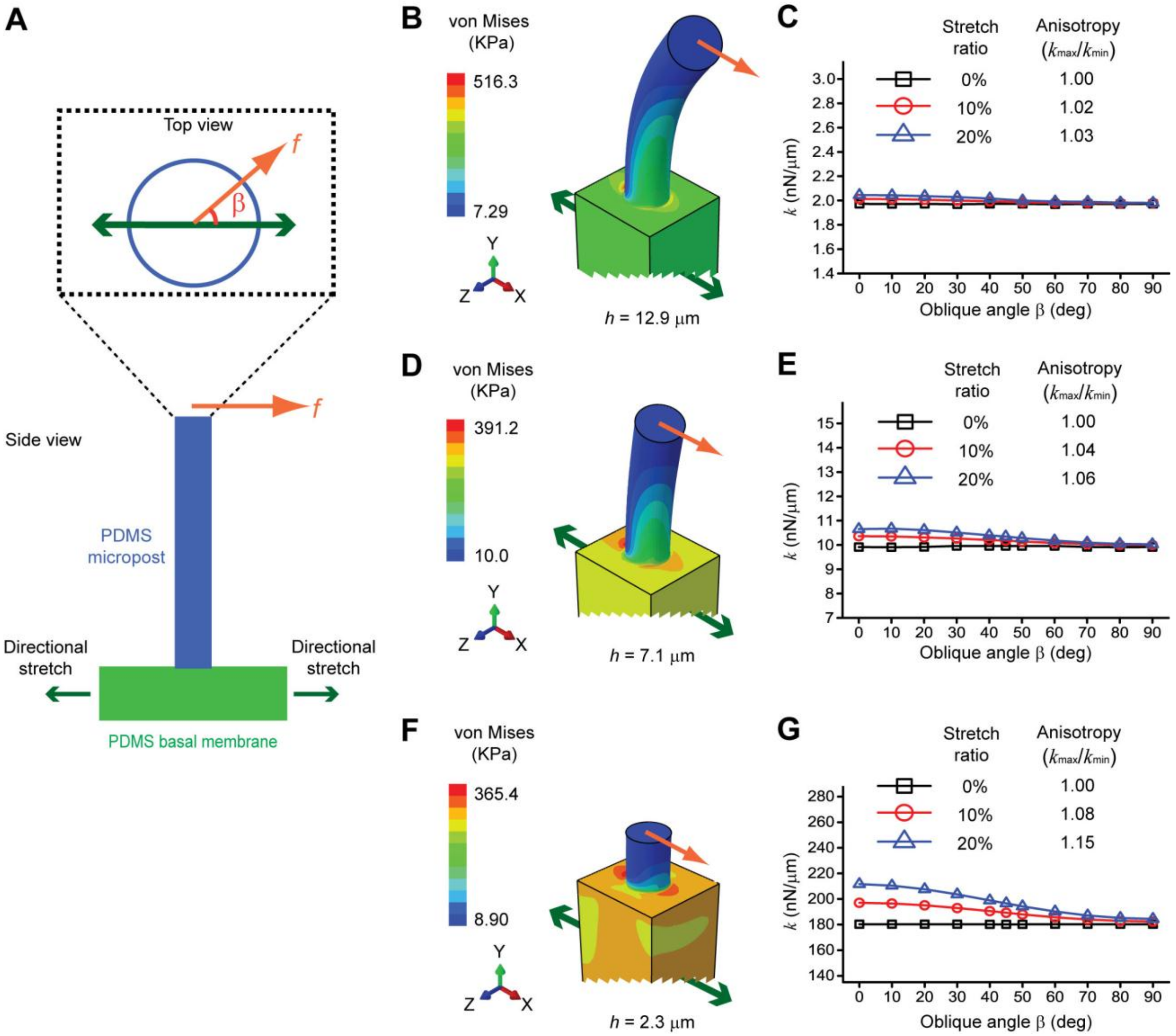

Supplementary Fig. S4. Finite element (FE) simulations of the anisotropy of the spring constant of the PDMS micropost on the PDMS basal membrane under uniaxial stretch. (**A**) Schematic of the FE model. A lateral force, *f*, of 15 nN (*orange arrow*) was applied to the top of the micropost. The PDMS basal membrane was subject to uniaxial stretch (*green arrows*) of 0%, 10% and 20%, respectively. An oblique angle, β, between the force *f* and the stretch direction was used to describe the anisotropy of the spring constant. (**B-G**) Representative 3D FE simulations of bending of the PDMS micropost of different heights (**B&C**: 12.9 µm; **D&E**: 7.1 µm; **F&G**: 2.3 µm) under the lateral force *f* (**B**, **D**, and **F**) and the resultant spring constant as function of the oblique angle β (**C**, **E**, and **G**). (*Inset table*) Calculated anisotropy of the micropost spring constant under different levels of stretch as indicated.

Supplementary Figure S5

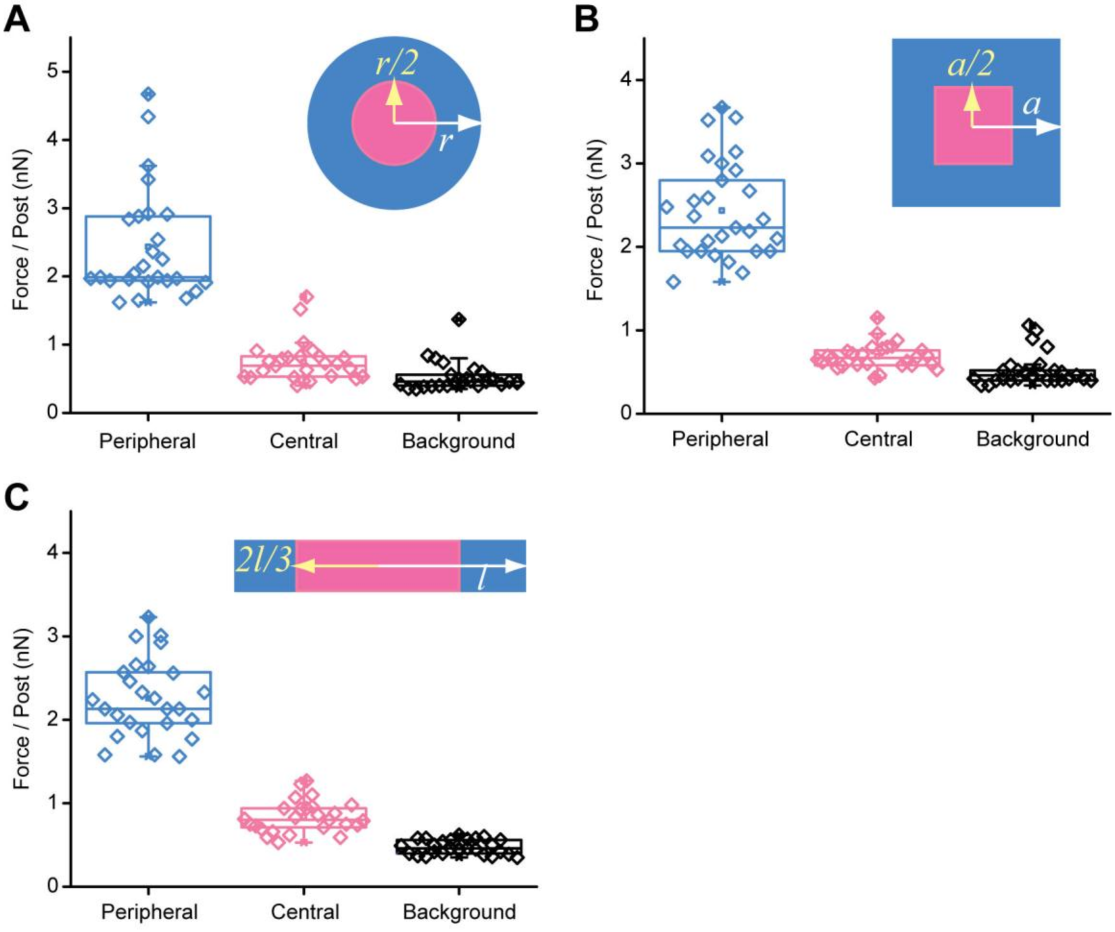

Supplementary Fig. S5. Spatial segregation of cellular cytoskeleton (CSK) contractile forces. Box-charts of cellular contractile force per micropost in the peripheral (*blue*) and central (*pink*) regions of cells conformed to circular (**A**; $n = 26$), square (**B**; $n = 28$) and rectangular (**C**; $n = 26$) adhesive islands. Background level of force per micropost was shown for comparison. (*Insets*) Schematics of spatial segregation in cells conformed to circular (**A**), square (**B**) and rectangular (**C**) adhesive islands.

Supplementary Figure S6

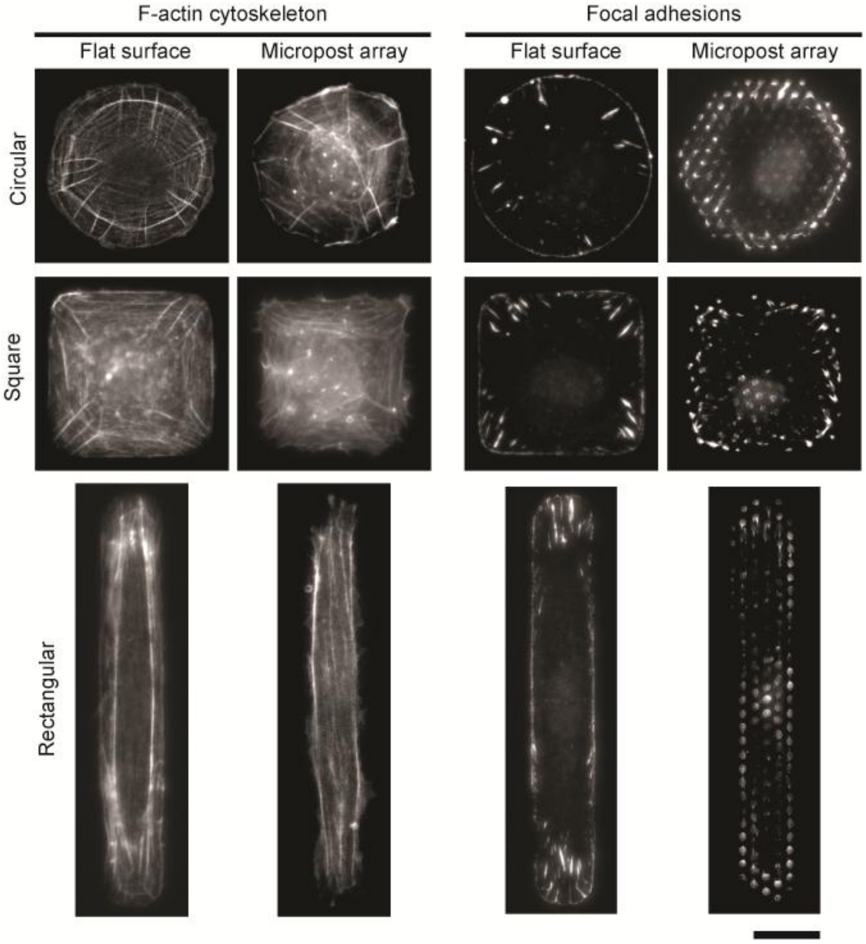

Supplementary Fig. S6. Comparative studies of the F-actin cytoskeleton (CSK; *left*) and focal adhesions (FAs; *right*) in single HUVECs of circular (*top*), square (*middle*) and rectangular (*bottom*) shapes cultured on flat PDMS surfaces and PDMS micropost arrays, as indicated. Scale bar, 20 µm.

Supplementary Figure S7

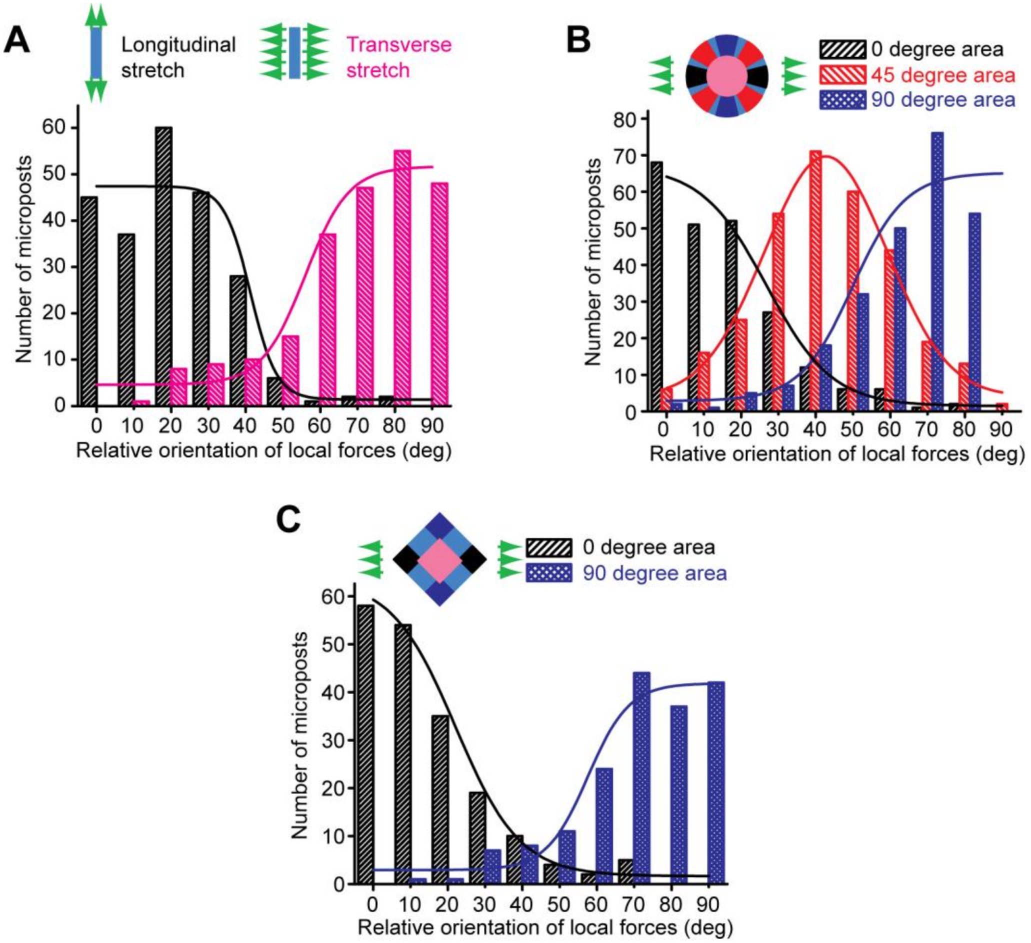

Supplementary Fig. S7. Statistical distributions of relative orientation of subcellular contractile forces with respect to uniaxial stretch direction in single HUVECs of different shapes (**A**: rectangle, and *n* = 10 for both longitudinal and transverse stretches; **B**: circular, and *n* = 15; **C**: square, *n* = 11). Given the background force level shown in **Supplementary Fig. S5**, only microposts with cellular contractile forces greater than 1 nN were analyzed. 0 degree means that local contractile force was in parallel with stretch, whereas 90 degree means local force was in perpendicular with stretch. Fitting curves were plotted for guidance of eyes.

Supplementary Figure S8

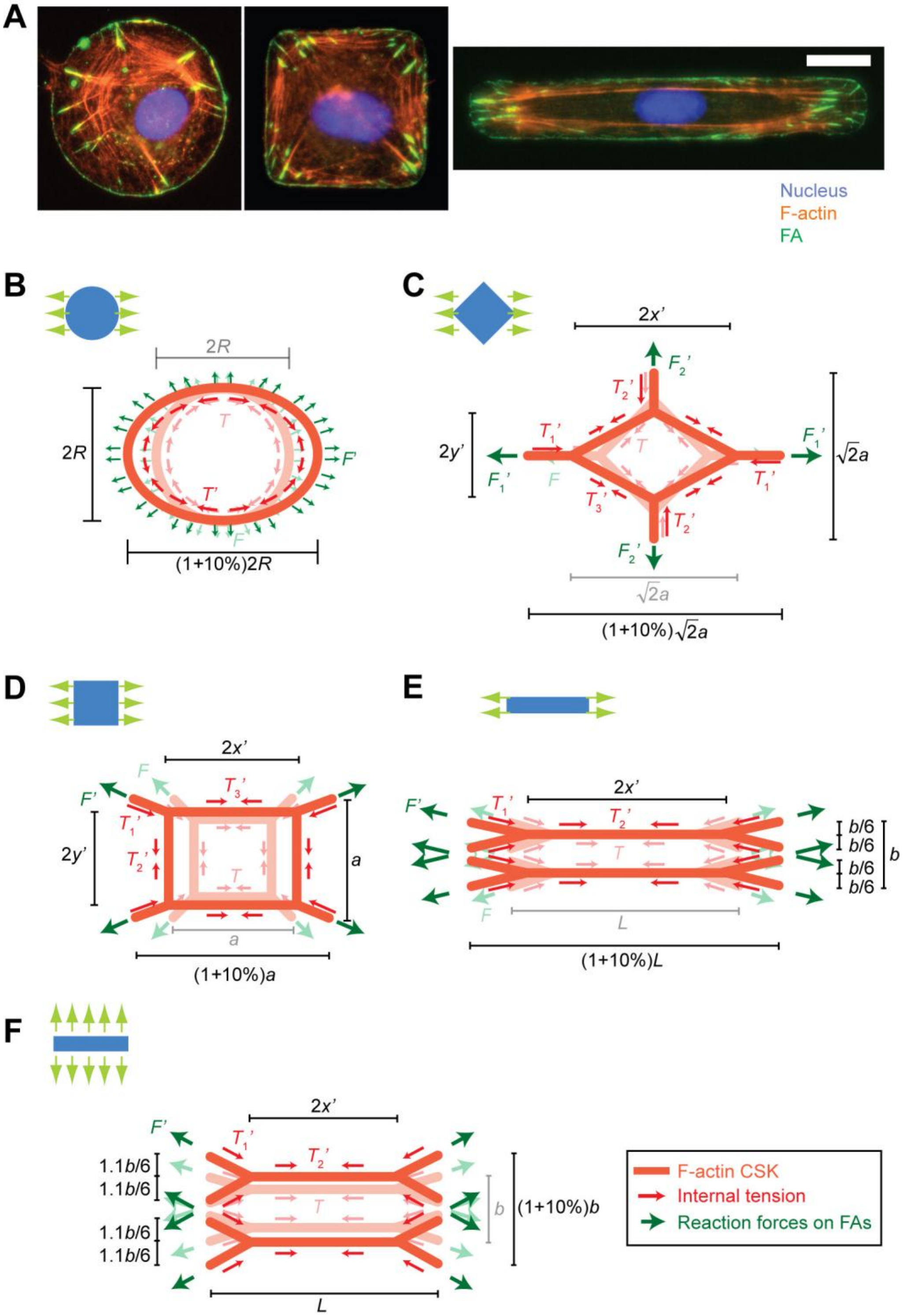

Supplementary Fig. S8. Theoretical modeling. (**A**) Immunofluorescence of the F-actin CSK structure and FAs in single HUVECs of circular (*left*), square (*middle*) and rectangular (*right*) shapes. Both radial and circumferential stress fibers were visible in circular- and square-shaped cells, whereas only highly aligned stress fibers were seen in rectangle-shaped cells. In circular- and square-shaped HUVECs, radial stress fibers extended into cell peripheries and connected to FAs, and circumferential stress fibers integrated these radial stress fibers into a global mechanical architecture. (**B-F**) Schematics of theoretical models for circular-shaped cells (**B**), square-shaped cells under diagonal (**C**) and side (**D**) stretches, and rectangular-shaped cells under longitudinal (**E**) and transverse (**F**) stretches. Stretched CSK architectures were depicted in dark red color, whereas reference CSK configurations were shown in light red color. For clarity, pre-stressed CSK configuration was not shown, which was topologically similar to the stretched configuration but only different in some length dimensions (*i.e.*, there was no stretch, or 0% stretch, in pre-stressed configuration). Given their similarity in topology and theoretical solutions, unknown variables in the stretched configuration were differentiated from those in the pre-stressed configuration only by the prime (’) on their top right corners.